

Article

# Role of Internal Radiation in Oxide Crystal Growth by Heat Exchanger Method

Wencheng Ma and Lijun Liu \*

Key Laboratory of Thermo-Fluid Science and Engineering, Ministry of Education,  
School of Energy and Power Engineering, Xi'an Jiaotong University, Xi'an 710049, Shaanxi, China;  
mawc.xjtu@stu.xjtu.edu.cn

\* Correspondence: ljliu@mail.xjtu.edu.cn; Tel./Fax: +86-29-82663443

Academic Editor: Bing Gao

Received: 18 October 2016; Accepted: 5 January 2017; Published: 9 January 2017

**Abstract:** Internal radiation was investigated using the finite volume method for the heat exchanger method (HEM) growth of oxide crystals. Special attention was devoted to the temperature and thermal stress distributions in the bottom region of the grown crystal at the end of the solidification process. The numerical results show that internal radiation strongly strengthens heat transport through the crystal. However, it causes isotherms to intensively concentrate in the crystal bottom region, leading to a significant increase in the temperature gradient and thermal stress in this region. Then, the effect of absorption coefficient on this phenomenon was numerically investigated. It was found that the radiation heat transfer rate at the bottom surface of the crystal monotonically decreases as the absorption coefficient is increased, while the conduction heat transfer rate first increases and then decreases as the absorption coefficient is increased, under the interaction between internal radiation and heat conduction. The variations of the maximum temperature gradient and thermal stress in the crystal bottom show the same tendency as the conduction heat transfer rate. This study indicates that the role of internal radiation on the heat transfer and thermal stress in oxide crystal by HEM process shows some differences from that by Czochralski and Kyropoulos processes.

**Keywords:** numerical simulation; internal radiation; oxide crystal; heat exchanger method; thermal stress

## 1. Introduction

Oxide single crystals, such as sapphire, gadolinium gallium garnet (GGG), yttrium aluminum garnet (YAG), and bismuth germanate (BGO), are widely utilized for manufacturing substrates, laser and various optical devices for science research and industry. Generally, oxide crystals are semitransparent to some extent to infrared heat radiation and work as participating medium in the growth systems. Radiation absorption and emission in participating crystals, known as internal radiation, significantly influences heat transfer in the crystal and melt. It is experimentally well-known that internal radiation leads to a deeply convex melt-crystal interface shape toward the melt in Czochralski (Cz) oxide crystal growth process [1,2]. Comprehensive understanding and accurate control of heat transfer in the crystal growth furnaces are essential to produce high-quality oxide single crystals, while internal radiation remains a major challenging issue. Considering the fact that the time-consuming and expensive experiments can only collect few required information in the high temperature environment due to the high melting point of the oxide crystals, numerical simulation is definitely an effective tool to accurately predict internal radiation heat transfer in the oxide crystal growth furnaces.

Research efforts in internal radiation in oxide crystal and melt are intense and ongoing. However, most of the numerical studies in the literature were devoted to Cz [3–11] and Kyropoulos (Ky) [11–15] processes, which are not referenced in detail here. Directional solidification (DS) techniques, such

as heat exchanger method (HEM), gradient solidification method (GSM) and vertical Bridgman (VB) method, are also widely used to produce oxide single crystals. Internal radiation in numerical investigations of heat transfer in the DS-like systems is typically ignored [16,17], or approximated as an artificially enhanced thermal conductivity [18,19]. In some other studies, internal radiation was dealt with by  $P_1$ -approximation [20–22] or treated as a surface phenomenon [23,24] assuming that the oxide crystal is totally transparent and internal radiation only acts between surfaces. Some researchers took into account internal radiation rigorously in their simulations [25–31]. For instance, Brandon and Derby [25,26] performed the first modeling of internal radiation heat transfer in oxide crystal by VB process using a rigorous finite element method and found that the absorption coefficient significantly affects the position and curvature of the melt-crystal interface. Xiong et al. [27] accounted for internal radiation by the discrete exchange factor method in their numerical investigation of a modified HEM crystal growth process. Ma and Wu et al. [28–30] established global heater transfer model, taking into account internal radiation by the finite volume method (FVM), for sapphire crystal growth by HEM and investigated the effects of crucible cover and crucible location on heat transfer during the solidification process. Miyagawa et al. [31] performed numerical simulations, considering internal radiation by a combination of ray tracing and discrete ordinate (DO) approach, for the seeding interface shapes during the VB process for sapphire crystal. Most of the above referenced numerical studies mainly focused on the effect of internal radiation on the melt-crystal interface and melt convection during the oxide crystal growth process by the DS-like techniques. The bottom surface of semitransparent oxide crystal directly contacts with the crucible during the solidification process and works as a heat sink in the DS-like techniques. Internal radiation can cause high temperature gradient and consequent high thermal stress in the bottom region of oxide crystal. However, thus far, there is no detailed report in the literature on this phenomenon. Besides, the effect of absorption coefficient on this phenomenon is still not understood.

The purpose of this study is to clarify the role of internal radiation on heat transfer and thermal stress in the oxide crystal by the DS-like techniques, taking a HEM furnace as an example. Internal radiation was modeled with the rigorous FVM. Global steady simulations of heat transfer with and without internal radiation in the crystal were firstly carried out for the end of the crystal solidification process. Based on the results of thermal field, thermal stress in the crystal was calculated and analyzed. Thermal stress is represented by the von Mises stress. Then, calculations were performed for a wide range of absorption coefficient to examine its effect on heat transfer and thermal stress in the crystal. Special attention was given to temperature and thermal stress fields in the bottom region of the oxide crystal.

## 2. Model Description

HEM is a typical DS-like technique for growing oxide single crystal and is chosen to perform the numerical simulation in the present study. The schematic diagram of the HEM furnace is given in Figure 1. The HEM furnace mainly consists of tungsten resistance heater, crucible, radiation shield and heat exchanger shaft. The dimension of the tungsten crucible is  $270 \text{ mm}^{\text{I.D.}} \times 420 \text{ mm}^{\text{H}} \times 20 \text{ mm}^{\text{T}}$ . The crucible was supported by the heat exchanger shaft filled with cooling helium flow. The cylindrical thermal radiation shields are made of a multitude of closely spaced, parallel, highly reflective tungsten slices, surrounding the heater and crucible to prevent heat loss from the furnace. The furnace is well sealed with a water-cooled wall and operates in an argon atmosphere with a very low pressure. Crystal solidification is maintained under a suitable temperature gradient by adjusting the heating power and the cooling helium flow rate. The height of the grown crystal is 216 mm.

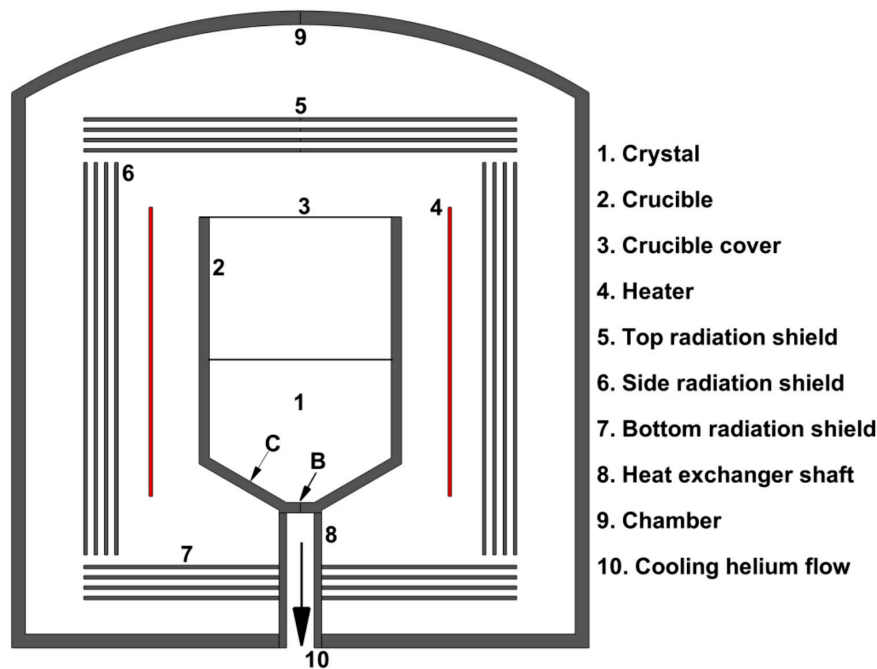


**Figure 1.** Schematic diagram of the heat exchanger method (HEM) furnace.

### 2.1. Modeling of Global Heat Transfer and Internal Radiation

In the present study, we mainly focus on the effect of internal radiation on heat transfer and thermal stress in the oxide crystal rather than on the melt-crystal interface and melt convection during the solidification process. For the sake of analysis and time-saving, global steady heat transfer model, taking into account thermal conduction, thermal radiation between solid surfaces, and internal radiation in the crystal as well as cooling helium flow in the heat exchanger shaft, was carried out for the end of the solidification process when the oxide melt was just completely solidified. To compromise between computational accuracy and convenience, the following assumptions were made in the current global model: (1) the furnace configuration is axisymmetric; (2) the radiative surfaces of all solids are diffuse-gray; (3) oxide crystal is assumed to be a gray medium, i.e., the absorption coefficient is independent of wavelength, and the scattering effect is ignored; and (4) the helium gas in the heat exchanger shaft is ideal and completely transparent. A structured/unstructured combined mesh scheme is applied in our simulations due to the presence of the irregular argon domain. The cooling helium flow in the heat exchanger shaft was assumed to be laminar as the Reynolds number at the inlet is about 1400. The algorithms for the global modeling of heat transfer in a crystal growth furnace have been described in our previous paper [32].

The energy conservation equation governing the thermal fields in the solid domains (except crystal) is written as:

$$\nabla \cdot (k\nabla T) + \dot{q} = 0 \quad (1)$$

where  $k$  is the thermal conductivity,  $T$  is the temperature, and  $\dot{q}$  is the heat source per unit volume in the heater and equals zero for all other solid components, including crucible, radiation shields, heat exchanger shaft and chamber wall.

The governing equations for the oxide crystal domain can be expressed in the following forms:

$$\nabla \cdot (k\nabla T) - \nabla \cdot \vec{q}_{rad} = 0 \quad (2)$$

The second term on the right-hand side in Equation (2) is the contribution of internal radiation, which is modeled by FVM [33]. Along a particular direction  $\vec{s}$ , the radiative transfer equation is expressed as:

$$\nabla \cdot \left( I(\vec{r}, \vec{s}) \vec{s} \right) + aI(\vec{r}, \vec{s}) = an'^2 I_b \quad (3)$$

where  $I$  is the radiation intensity at position  $\vec{r}$  in direction  $\vec{s}$ ,  $a$  is the absorption coefficient,  $n'$  is the refractive index, and  $I_b$  is the black intensity. Since the radiation intensity is the function of the location and direction, both spatial and angular domains need to be discretized to numerically solve the radiative transfer equation. The spatial discretization for radiation calculation in the crystal is the same as that for the temperature field calculation. The  $4\pi$  angular domain at any spatial location is discretized into  $M = N_\theta \times N_\varphi$  discrete nonoverlapping solid angles. The polar angle  $\theta$  and azimuthal angle  $\varphi$ , which are measured with respect to the global Cartesian system, are equally divided into  $N_\theta$  and  $N_\varphi$  parts. In the FVM, the radiative transfer equation is transformed into a set of simultaneous partial differential equation. The basic assumption of the FVM is that the radiation intensity is constant within the control volume and over the control angle. Thus, the radiative heat flux  $\vec{q}_{rad}$  in Equation (2) can be written as follows:

$$\vec{q}_{rad} = \int_{4\pi} I(\vec{r}, \vec{s}) \cdot \vec{s} d\Omega = \sum_{i=1}^M I(\vec{r}, \vec{s}) \int_{\Delta\Omega_i} \vec{s}_i d\Omega_i \quad (4)$$

where  $\Omega$  is the solid angle, and  $M$  is the number of the discrete solid angles. Ray effect is a fundamental shortcoming of the FVM for radiation calculation. It is a consequence of angular discretization and leads to unphysical results [34]. Therefore, a high degree angular discretization of  $M = N_\theta \times N_\varphi = 8 \times 16$  for the  $4\pi$  angle domain is applied to mitigate the ray effect in this study, which has been proved to be numerical acceptable in our previous study [35].

## 2.2. Modeling of Thermal Stress

The displacement-based thermo-elastic stress model [36] was used to analyze the thermal stress distribution in the oxide crystal. The Von Mises stress is applied to represent the thermal stress and defined as follows:

$$\sigma_{von} = \sqrt{\frac{3}{2} S_{ij} S_{ij}} \quad (5)$$

$$S_{ij} = \sigma_{ij} - \frac{1}{3} \sigma_{kk} \delta_{ij} \quad (6)$$

where  $\sigma_{von}$  is the Von Mises stress,  $S_{ij}$  is the stress deviator tensor,  $\sigma_{ij}$  is the stress tensor, and  $\delta_{ij}$  is the Kronecker delta. The governing equation for the stress balance can be written as:

$$\partial\sigma_{ij}/\partial x_j = 0 \quad (7)$$

The stress–strain relation can be described as:

$$\sigma_{ij} = 2\kappa\xi_{ij} + \lambda\delta_{ij}\xi_{kk} - (3\lambda + 2\kappa)\beta\delta_{ij}(T - T_m) \quad (8)$$

where  $\kappa$  and  $\lambda$  are Lamé's constants,  $\beta$  is the thermal expansion coefficient of the sapphire crystal, and  $\xi_{ij}$  is the strain tensor. Lamé's constants,  $\kappa$  and  $\lambda$ , can be described as follows:

$$\kappa = \frac{E}{2(1+\nu)} \quad (9)$$

$$\lambda = \frac{\nu E}{(1+\nu)(1-2\nu)} \quad (10)$$

where  $E$  is the elastic modulus and  $\nu$  is Poisson ratio. The geometry equation can be given as:

$$\xi_{ij} = \frac{1}{2} \left( \frac{\partial U_i}{\partial x_j} + \frac{\partial U_j}{\partial x_i} \right) \quad (11)$$

where  $U_i$  is the displacement with respect to the direction  $x_i$ .

### 2.3. Boundary Conditions

All domains in the furnace are fully coupled in our simulations. Temperature continuity and heat flux conservation are kept at all interior boundaries between any two different domains. For the interfaces between the solid components and the gas domains, the thermal boundary condition can be expressed as:

$$-k_g(\nabla T)_g \cdot \vec{n} + k_s(\nabla T)_s \cdot \vec{n} + \vec{q}_{rad} \cdot \vec{n} = 0 \quad (12)$$

$$T_g = T_s \quad (13)$$

where the subscripts  $g$  and  $s$  represent gas and solid, respectively.  $\vec{n}$  is the unit normal vector at the boundaries.  $\vec{q}_{rad}$  is the radiative heat flux at the gas side. For the interface between the crucible and the crystal, the thermal boundary condition is given as:

$$-k_{cry}(\nabla T)_{cry} \cdot \vec{n} + k_{cru}(\nabla T)_{cru} \cdot \vec{n} + \vec{q}_{rad} \cdot \vec{n} = 0 \quad (14)$$

$$T_{cry} = T_{cru} \quad (15)$$

where the subscripts  $cry$  and  $cru$  represent crystal and crucible, respectively.  $\vec{q}_{rad}$  is the radiative heat flux at the crystal side.

No-slip and non-penetration conditions are applied for all walls in the helium flow domain. At the inlet of the heat exchanger shaft, the same volume flow rate is fixed for all cases. The inlet temperature and pressure are set to 300 K and 24 PSI, respectively. All gas variables are extrapolated from the interior points at the outlet boundary of the helium flow domain. The temperature of the outer wall of is assumed to be 300 K due to the efficient cooling water in the furnace chamber wall. For the symmetry axis, the boundary conditions are described as:

$$u_n = 0, \quad \frac{\partial u_\tau}{\partial n} = 0, \quad \frac{\partial T}{\partial n} = 0 \quad (16)$$

where  $u$  is the velocity. The subscripts  $\tau$  and  $n$  represent tangential and normal directions, respectively. For a diffuse-gray surface, the boundary condition for radiation intensity  $I$  is given as:

$$I(\vec{r}, \vec{s}_i) = \epsilon n'^2 \frac{\sigma' T_w^4}{\pi} + \frac{1-\epsilon}{\pi} \int_{\vec{n} \cdot \vec{s} < 0} I(\vec{r}, \vec{s}) \cdot |\vec{n} \cdot \vec{s}| d\Omega \quad (17)$$

where  $\epsilon$  is the surface emissivity,  $\sigma'$  is the Boltzmann constant, and  $T_w$  is the surface temperature.

For the calculation of thermal stress in oxide crystal, the free boundary condition is applied to all boundaries except the symmetry axis, which can be described as:

$$\vec{\sigma} \cdot \vec{n} = 0 \quad (18)$$

## 3. Results and Discussion

### 3.1. Grid Independence

In this study, we consider the growth of an oxide crystal whose physical properties similar to those of sapphire crystal, except for the absorption coefficient, varying in a wide range in the

numerical simulations. The major thermophysical properties of materials are available from our previous work [28,30] and are listed in Table 1.

**Table 1.** Thermophysical properties of materials.

Description	Value
Density(kg/m <sup>3</sup> ):	
crystal	3000
tungsten	19,350
steel	7600
Thermal conductivity (W/(m·K)):	
crystal	5.8
tungsten	174
steel	70
helium	$0.067 + 3.2 \times 10^{-5} \times T - 4.0 \times 10^{-8} \times T^2$
Heat capacity(J/(kg·K)):	
crystal	765
tungsten	130
helium	5200
steel	1000
Dynamic viscosity (kg/(m·s)):	
helium	$5.58 \times 10^{-5}$
Emissivity:	
crystal	0.9
tungsten	0.3
steel	0.2
Other properties:	
thermal expansion of crystal (K <sup>-1</sup> )	$5.0 \times 10^{-6}$
absorption coefficient of crystal (m <sup>-1</sup> )	0–1900
refractive index of crystal	1.78
elastic modulus of crystal (GPa)	430
poison ratio of crystal	0.28

The crystal domain is meshed with  $79 \times 112$  structured elements in radial and axial directions, respectively, with refined boundary layers to account for the high spatial resolution at the crystal-crucible boundary due to the internal radiation effect. The grid independence study has been conducted using maximum temperature gradient and radiation heat transfer rate (integration of radiation heat flux along the surface) at the bottom central surface (marked by B in Figure 1) of the crystal as sensitivity parameters. The results show that the maximum temperature gradient and radiation heat transfer rate, for the crystal with a absorption coefficient of  $19 \text{ m}^{-1}$ , was only varied by relative values of 3.1% and 1.2%, respectively, when the grid were refined to  $204 \times 292$  elements. Therefore, the gird of  $79 \times 112$  elements for the crystal domain is numerically acceptable and is applied in the present study.

### 3.2. With and without Internal Radiation

To investigate the effect of internal radiation on heat transfer and thermal stress in the oxide crystal by HEM process, numerical calculations for the crystal with and without internal radiation were firstly performed in this section. Here, the absorption coefficient was set to be  $19 \text{ m}^{-1}$  for the case with internal radiation, which is illustrated as “with IR”. The case without internal radiation is illustrated as “without IR”. Heating power in the heater was automatically iterated to achieve that the maximum temperature of the crystal is slightly lower (about 0.1 K) than the melting point. Figure 2

shows the temperature and thermal stress distributions in the crystal at the end of the solidification process for both cases. Figure 3 presents the heat flux distribution along the bottom surfaces (marked by B and C in Figure 1) of the crystal for both cases. Generally, heat is transported into the crystal from the top and side surfaces and out from the bottom surface in a HEM furnace. When internal radiation is not considered, the crystal is opaque and only heat conduction occurs. The conduction heat flux along the bottom surfaces is relatively small with a conduction heat transfer rate of 31.6 W at the surface B. It was found that the isotherms in the crystal present a convex shape with an axial temperature difference of 232 K, as shown in Figure 2a. When internal radiation is taken into account, there are two kinds of heat transfer in the crystal: internal radiation and heat conduction. The total (conduction plus radiation) heat flux is significantly increased with a total heat transfer rate of 335.3 W at the surface B, which is more than a factor of ten over the case without internal radiation. Besides, the results also show a ratio of about 2 between the radiation and conduction heat fluxes along the surface B. This means that internal radiation enhances and dominates heat transport in the oxide crystal, resulting in a smaller axial temperature difference of 116 K, compared to the crystal without internal radiation. The isotherms are significantly sparse in the main body and intensively concentrated in the bottom region of the crystal due to the radiation cooling, as the bottom surface of the crystal works as a heat sink in the HEM furnace. Besides, the isotherms present a convex–concave shape at the conical region of the crystal, as shown in Figure 2b. For both cases, high thermal stress is located in the bottom region of the crystal. However, the maximum thermal stress in the crystal with internal radiation is much higher than that without internal radiation.

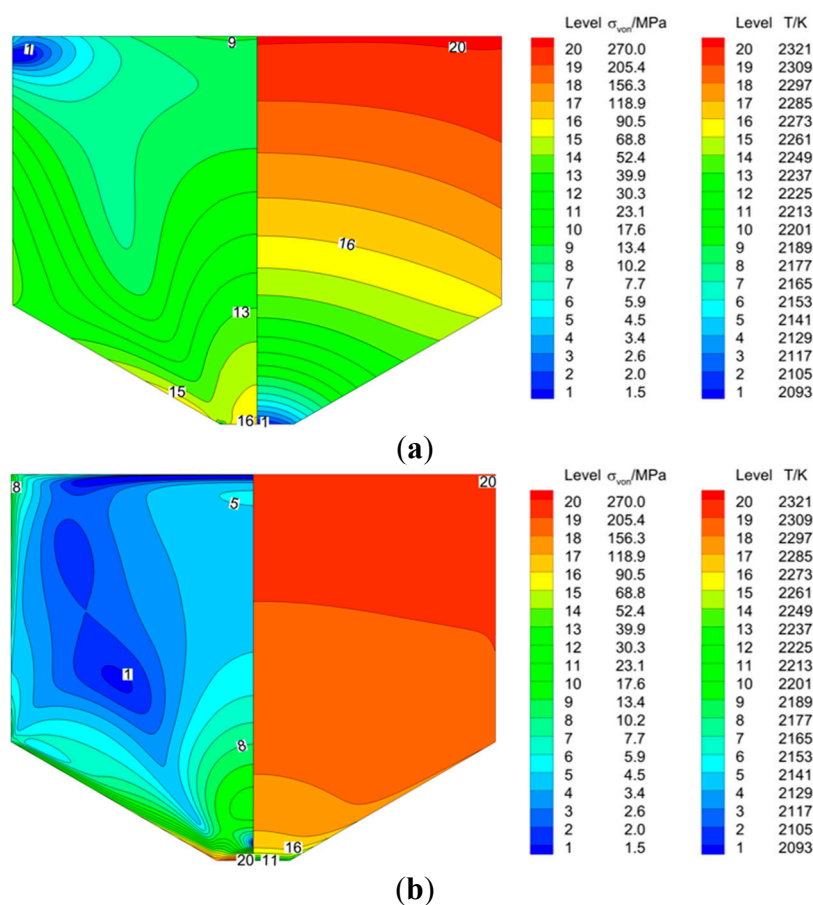


**Figure 2.** Temperature (right) and thermal stress (left) distributions in the crystal: (a) without; and (b) with internal radiation at the end of the solidification process.

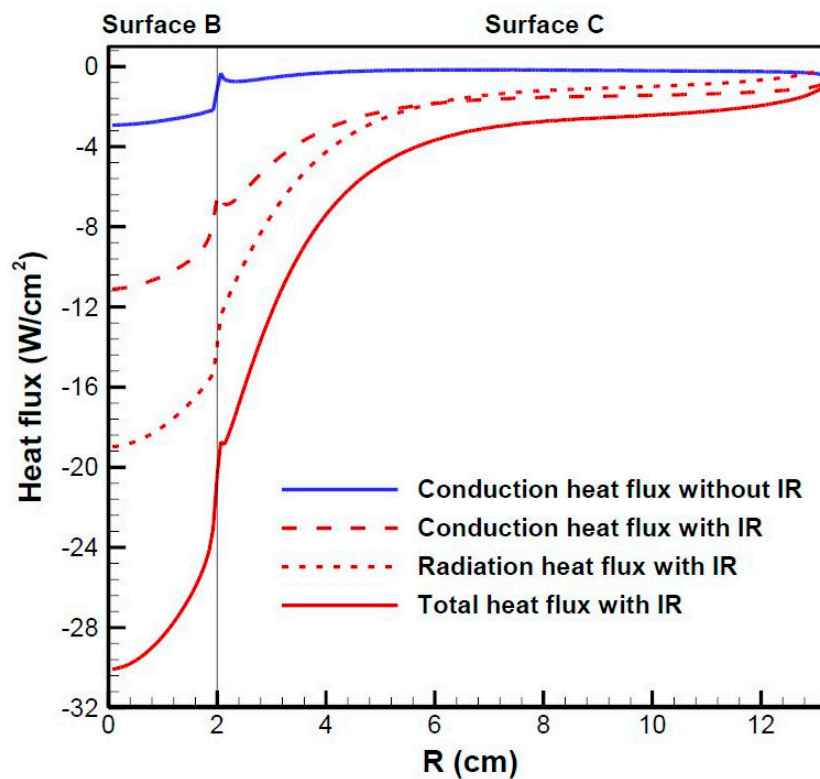
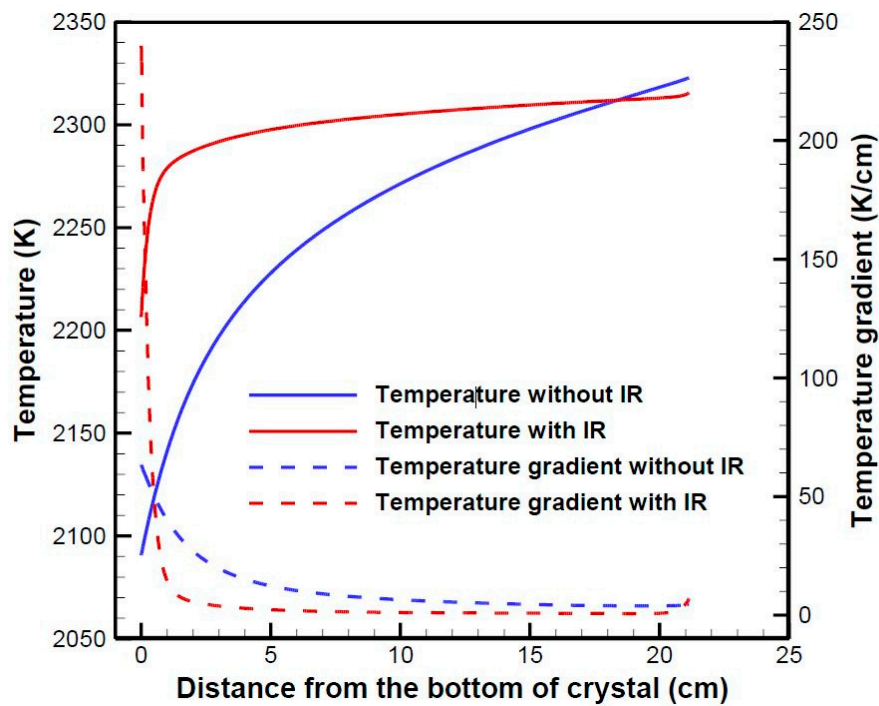
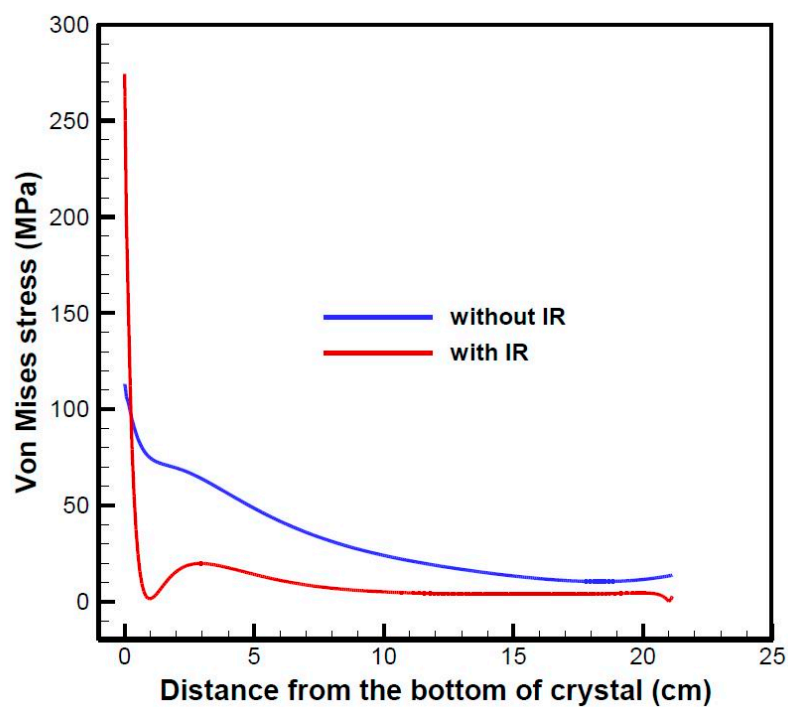


**Figure 3.** Heat flux distributions along the bottom surfaces of the crystal without and with internal radiation.

Temperature and temperature gradient along the centerline of the crystal in Figure 2 are extracted and presented in Figure 4a. The results show that temperature and temperature gradient vary gently along the centerline of the crystal without internal radiation. However, the variation of temperature is mainly located in the relatively narrow bottom region of the crystal, leading to a significant increase in the temperature gradient in this region with a maximum value of 242.6 K/cm, for the crystal with internal radiation. This phenomenon can be explained by the following way. In the present steady state study, the total heat transported into the semitransparent oxide crystal from the top and side surfaces is equal to that out the crystal from the bottom conical and central surfaces. When the radiation heat passes through the oxide crystal, part of it will be absorbed and converted into internal energy, i.e., conduction heat. Thus, that the radiation heat decreases and the conduction heat increases at the bottom surfaces to maintain the energy conservation, leading to a large temperature gradient in the bottom region. This argument also explains the observation that the conduction heat flux along the surface B of the crystal with internal radiation is significantly larger than that without internal radiation, as shown in Figure 3. Figure 4b illustrates the thermal stress along the centerline of the crystal for both cases. We can find that the thermal stress in the main body of the crystal with internal radiation is lower than that without internal radiation, due to the smaller temperature gradient in this region, as shown in Figure 4a. However, it sharply increases in the narrow bottom region to a maximum value of 274 Mpa, which is more than twice that without internal radiation.



(a)



(b)

**Figure 4.** Temperature, temperature gradient (a); and thermal stress (b) along the centerline of the crystal in Figure 2.

It is worth noting that the effect of internal radiation in the oxide crystal by HEM shows some differences from that by Cz and Ky processes. For instance, Tsukada et al. [3,7] pointed out that internal radiation decreases the temperature gradient in the oxide crystal in a Cz furnace. Fang et al. [15] stated that internal radiation uniformizes the temperature distribution and reduces the stress level in

the sapphire crystal in a Ky furnace. That is to say, internal radiation does not cause local significant high temperature gradient and thermal stress in the oxide crystal by Cz and Ky growth processes as it does in the crystal by HEM process. The reason is that the top surface of an oxide crystal is generally thought as a transparent surface in the Cz and Ky furnaces and internal radiation heat can directly pass through it without causing isotherms concentrated near the surface. While the bottom surface directly contacts with the crucible in the HEM furnace and is treated as an opaque surface in this study.

### 3.3. Effect of Absorption Coefficient

Internal radiation in semitransparent oxide crystal depends largely on the absorption coefficient. In this section, numerical calculations were carried out for a wide range of absorption coefficient to examine its effect on heat transfer and thermal stress in the crystal. Figure 5 shows the temperature and thermal stress distributions in the crystal with different absorption coefficients. For the case of  $a = 0 \text{ m}^{-1}$ , the crystal is totally transparent and radiation heat just passes through the crystal without directly coupling into the temperature field. The isotherms present a similar convex shape as the crystal without internal radiation, with a much smaller temperature difference due to the strongly enhanced heat transfer ability. As the absorption coefficient increases, the isotherms are gradually concentrated in the bottom region of the crystal under the interaction between internal radiation and heat conduction. Besides, the isotherms gradually change into a convex–concave shape at the conical region of the crystal. As the absorption coefficient further increases, internal radiation heat transfer becomes weak and heat conduction gradually governs heat transport through the crystal. The concentration of isotherms in the bottom region is gradually released and the concave shape along the conical edge is gradually disappeared. The isotherms become similar to those of the crystal without internal radiation again. As the absorption coefficient increases, the thermal stress in the central region of the crystal first decreases and then increases.

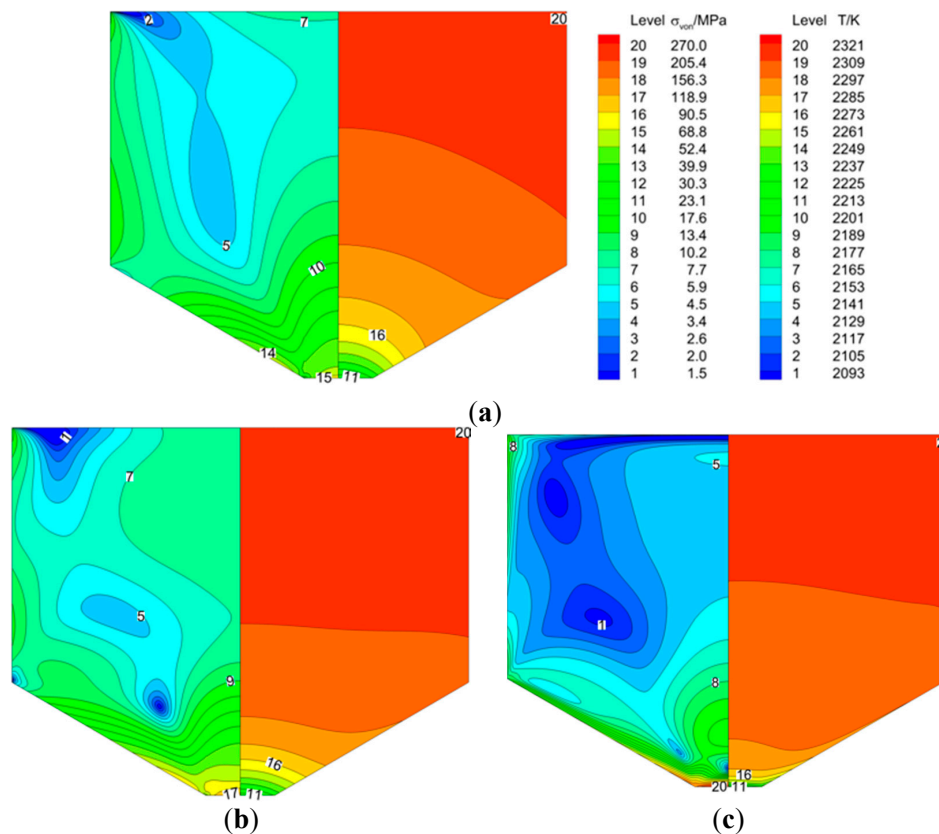
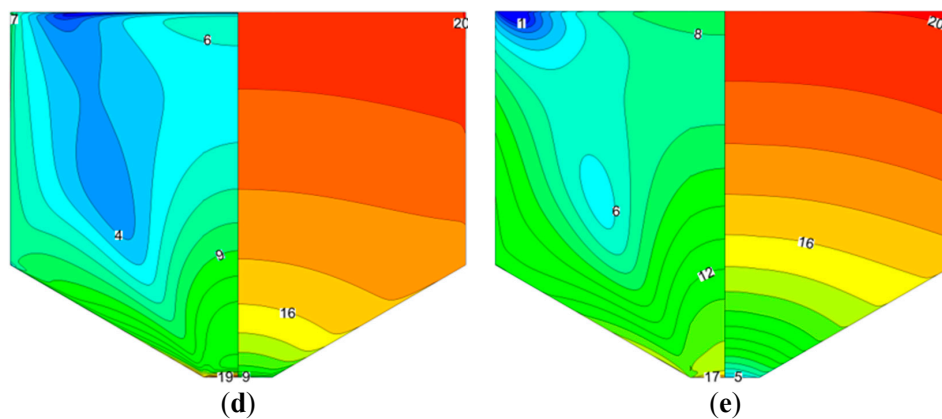
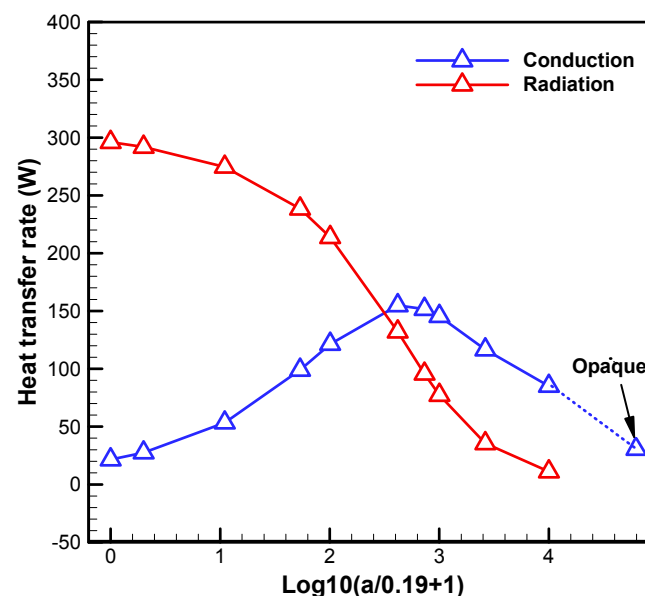


Figure 5. Cont.



**Figure 5.** Temperature (right) and thermal stress (left) distributions in the crystal with different coefficient absorptions: (a)  $a = 0 \text{ m}^{-1}$ ; (b)  $a = 0.19 \text{ m}^{-1}$ ; (c)  $a = 10 \text{ m}^{-1}$ ; (d)  $a = 79 \text{ m}^{-1}$ ; and (e)  $a = 500 \text{ m}^{-1}$ .

The variations of radiation and conduction heat transfer rates at the surface B with absorption coefficient are presented in Figure 6. The radiation heat transfer rate monotonically decreases with the increasing absorption coefficients due to the decreasing ability of internal radiation heat transfer, while the conduction heat transfer rate first increases and then decreases as the absorption coefficient increases. The variation of the conduction heat transfer rate as a function of absorption coefficient is understood in the following manner. When the absorption coefficient is relatively small, the increasing conduction heat rate is a result of more radiation heat absorbed by the crystal with the increasing absorption coefficient. As the absorption coefficient further increases, internal radiation strongly weakens, leading to less radiation heat to be absorbed by the crystal, so that the conduction heat transfer rate decreases.



**Figure 6.** Heat transfer rates at the bottom central surface of the crystal with different coefficient absorptions.

The variations of the maximum temperature gradient and maximum thermal stress at the bottom of the crystal with the changing absorption coefficient, as shown in Figure 7, present the same tendency as the conduction heat transfer rate does because the conduction heat transfer rate directly determines the temperature gradient. However, it is surprising that the peak values of the profiles of the maximum temperature gradient and maximum thermal stress are located at different absorption coefficients,

which are  $79 \text{ m}^{-1}$  and  $10 \text{ m}^{-1}$ , respectively. To explain this observation, the local distributions of the temperature gradient under these two absorption coefficients are compared in Figure 8. It was found that the temperature gradient under the absorption coefficient of  $10 \text{ m}^{-1}$  is larger than that of  $79 \text{ m}^{-1}$  for the most part of the bottom region of the crystal. The maximum thermal stress in the crystal can be indirectly considered as the accumulation of the thermal displacement under the effect of the temperature gradient. Therefore, the maximum thermal stress in the crystal under absorption coefficient of  $10 \text{ m}^{-1}$  is larger than that of  $79 \text{ m}^{-1}$ .

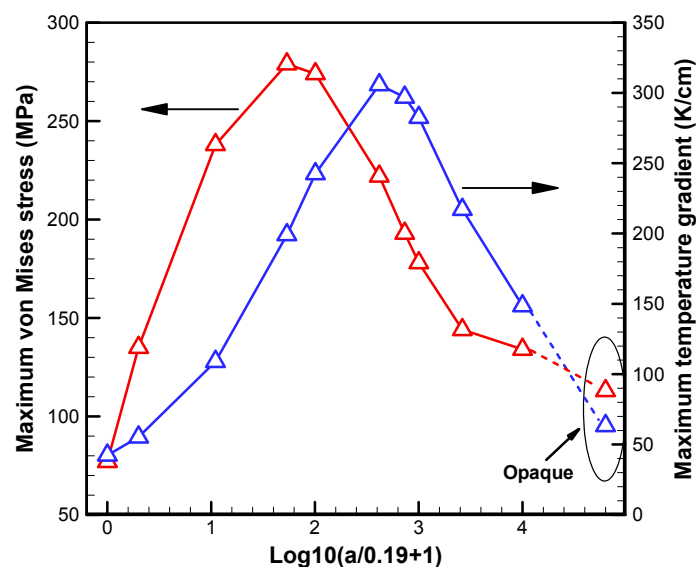


**Figure 7.** Maximum temperature gradient and thermal stress at the bottom of crystal with different coefficient absorptions.

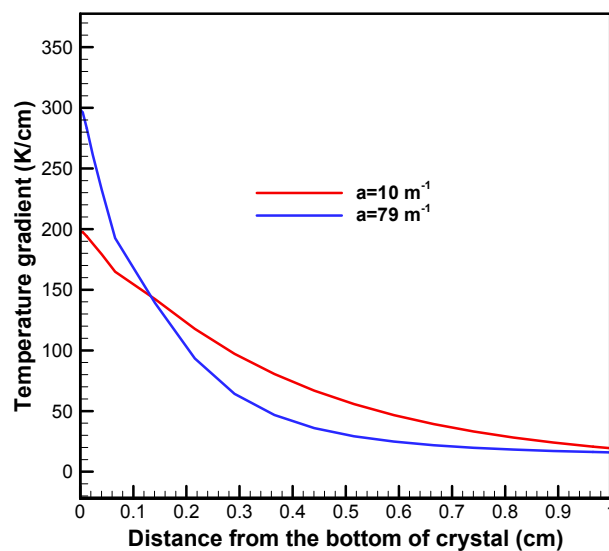


**Figure 8.** Local distribution of temperature gradient along the centerline of the crystal.

Although the previous discuss has focused on a HEM furnace, the conclusions in this study are also applicable to the oxide crystal growth process by other DS-like techniques, such as GSM and VB. This is based on the facts that the direction of heat transport in the oxide crystal is generally same for all the different kinds of DS-like processes and the bottom surface of the oxide crystal directly contacts with the crucible during the solidification process, working as a heat sink in the DS-like techniques.

#### 4. Conclusions

In this study, the effect of internal radiation on heat transfer and thermal stress in an oxide crystal by HEM process was numerically investigated based on a global heat transfer model. Internal radiation was incorporated into the global model by the FVM. The results show that internal radiation plays an important role in the oxide crystal growth. It strongly enhances the heat transport through the crystal, and reduces the temperature gradient and thermal stress in the central body of the crystal. However, internal radiation makes isotherms intensively concentrated in the bottom region of the crystal, leading to a significant increase in temperature gradient and thermal stress in this region due to the interaction of internal radiation and heat conduction. The absorption coefficient significantly affects internal radiation and heat conduction heat transfer in the oxide crystal, and consequently influences the temperature and thermal stress distributions in the crystal. It was found that the radiation heat transfer rate at the bottom surface of the crystal presents a monotonic decrease as the increasing absorption coefficient, while the conduction heat transfer rate first increases and then decreases as the absorption coefficient increases. The variations of the maximum temperature gradient and thermal stress at the bottom of the crystal with the changing absorption coefficient show the same tendency as the conduction heat transfer rate. Furthermore, the applicability of these main conclusions to the oxide crystal growth by other DS-like techniques was also discussed. This investigation indicates that the effect of internal radiation on the heat transfer and thermal stress in oxide crystal growth by HEM are different to some extent from that by Cz and KY techniques.

**Acknowledgments:** This research was supported by the National Natural Science Foundation of China (No. 51676154) and Natural Science Basic Research Plan in Shaanxi Province of China (No. 2014JZ014).

**Author Contributions:** Wencheng Ma is a doctoral student. He developed the models, carried out the simulations, analyzed the results and wrote the manuscript. Lijun Liu is Ma's supervisor and advisor on this research. He conceived the ideas, checked the analysis of the results and revised the manuscripts.

**Conflicts of Interest:** The authors declare no conflict of interest.

#### References

1. Cockayne, B.; Chesswas, M.; Gasson, D.B. Facetting and optical perfection in Czochralski grown garnets and ruby. *J. Mater. Sci.* **1969**, *4*, 450–456. [[CrossRef](#)]
2. Kvapil, Ji.; Kvapil, Jo.; Manek, B.; Perner, B.; Autrata, R.; Scuer, P. Czochralski growth of YAG:Ce in a reducing protective atmosphere. *J. Cryst. Growth* **1981**, *52*, 542–545. [[CrossRef](#)]
3. Tsukada, T.; Kakinoki, K.; Hozawa, M.; Imaishi, N. Effect of internal radiation within crystal and melt on Czochralski crystal growth of oxide. *Int. J. Heat Mass Transf.* **1995**, *38*, 2707–2714. [[CrossRef](#)]
4. Kobayashi, M.; Tsukada, T.; Hozawa, M. Effect of internal radiative heat transfer on transition of flow modes in Cz oxide melt. *J. Cryst. Growth* **2000**, *208*, 459–465. [[CrossRef](#)]
5. Nunes, E.M.; Naraghi, M.H.N.; Zhang, H.; Prasad, V. A volume radiation heat transfer model for Czochralski crystal growth processes. *J. Cryst. Growth* **2002**, *236*, 596–608. [[CrossRef](#)]
6. Yuferev, V.S.; Budenkova, O.N.; Vasiliev, M.G.; Rukolaine, S.A.; Shlegel, V.N.; Vasiliev, Y.V.; Zhmakin, A.I. Variations of solid-liquid interface in the BGO low thermal gradients Cz growth for diffuse and specular crystal side surface. *J. Cryst. Growth* **2003**, *253*, 383–397. [[CrossRef](#)]
7. Hayashi, A.; Kobayashi, M.; Jing, C.J.; Tsukada, T.; Hozawa, M. Numerical simulation of the Czochralski growth process of oxide crystals with a relatively thin optical thickness. *Int. J. Heat Mass Transf.* **2004**, *47*, 5501–5509. [[CrossRef](#)]
8. Banerjee, J.; Muralidhar, K. Role of internal radiation during Czochralski growth of YAG and Nd:YAG crystals. *Int. J. Therm. Sci.* **2006**, *45*, 151–167. [[CrossRef](#)]
9. Tavakoli, M.H. Numerical study of heat transport and fluid flow during different stages of sapphire Czochralski crystal growth. *J. Cryst. Growth* **2008**, *310*, 3107–3112. [[CrossRef](#)]
10. Fang, H.S.; Zhang, Q.J.; Tian, J.; Wang, S.; Ma, R.H. Study of internal radiation with solute inclusions during Czochralski sapphire crystal growth. *Int. J. Heat Mass Transf.* **2014**, *79*, 783–789. [[CrossRef](#)]

11. Demina, S.E.; Kalaev, V.V. 3D unsteady computer modeling of industrial scale Ky and Cz sapphire crystal growth. *J. Cryst. Growth* **2011**, *320*, 23–27. [[CrossRef](#)]
12. Demina, S.E.; Bystrova, E.N.; Lukanina, M.A.; Mamedov, V.M.; Yuferev, V.S.; Eskov, E.V.; Nikolenko, M.V.; Postolov, V.S.; Kalaev, V.V. Numerical analysis of sapphire crystal growth by the Kyropoulos technique. *Opt. Mater.* **2007**, *30*, 62–65. [[CrossRef](#)]
13. Demina, S.E.; Bystrova, E.N.; Postolov, V.S.; Eskov, E.V.; Nikolenko, M.V.; Marshanin, D.A.; Yuferev, V.S.; Kalaev, V.V. Use of numerical simulation for growing high-quality sapphire crystals by the Kyropoulos method. *J. Cryst. Growth* **2008**, *310*, 1443–1447. [[CrossRef](#)]
14. Lee, W.J.; Lee, Y.C.; Jo, H.H.; Park, Y.H. Effect of crucible geometry on melt convection and interface shape during Kyropoulos growth of sapphire single crystal. *J. Cryst. Growth* **2011**, *324*, 248–254. [[CrossRef](#)]
15. Fang, H.S.; Jin, Z.L.; Zhang, M.J.; Zhang, Z.; Zhao, C.J. Role of internal radiation at the different growth stages of sapphire by Kyropoulos method. *Int. J. Heat Mass Transf.* **2013**, *67*, 967–973. [[CrossRef](#)]
16. Lu, C.W.; Chen, J.C. Numerical computation of sapphire crystal growth using heat exchanger method. *J. Cryst. Growth* **2001**, *225*, 274–281. [[CrossRef](#)]
17. Chen, J.C.; Lu, C.W. Influence of the crucible geometry on the shape of melt-crystal interface during growth of sapphire crystal using a heat exchanger method. *J. Cryst. Growth* **2004**, *266*, 239–245. [[CrossRef](#)]
18. Vizman, D.; Nicoara, I.; Nicoara, D. On the factors affecting the isotherm shape during Bridgman growth of semi-transparent crystals. *J. Cryst. Growth* **1996**, *169*, 161–169. [[CrossRef](#)]
19. Barvinschi, F.; Bunoiu, O.; Nicoara, I.; Nicoara, D.; Santailier, J.L.; Duffar, T. Factors affecting the isotherm shape of semi-transparent BaF<sub>2</sub> crystals grown by Bridgman method. *J. Cryst. Growth* **2002**, *237–239*, 1762–1768. [[CrossRef](#)]
20. Lan, C.W.; Tu, C.Y.; Lee, Y.F. Effects of internal radiation on heat flow and facet formation in Bridgman growth of YAG crystals. *Int. J. Heat Mass Transf.* **2003**, *46*, 1629–1640. [[CrossRef](#)]
21. Backofen, R.; Bilz, T.; Ribalta, A.; Voigt, A. SP<sub>N</sub>-approximations of internal radiation in crystal growth of optical materials. *J. Cryst. Growth* **2004**, *266*, 264–270. [[CrossRef](#)]
22. Stelian, C. Numerical modeling of radiative heat transfer in Bridgman solidification of semi-transparent BaF<sub>2</sub> crystals. *J. Cryst. Growth* **2007**, *306*, 444–451. [[CrossRef](#)]
23. Brandon, S.; Gazit, D.; Horowitz, A. Interface shapes and thermal fields during the gradient solidification method growth of sapphire single crystals. *J. Cryst. Growth* **1996**, *167*, 190–207. [[CrossRef](#)]
24. Zhang, N.; Park, H.G.; Derby, J.J. Simulation of heat transfer and convection during sapphire crystal growth in a modified heat exchanger method. *J. Cryst. Growth* **2013**, *367*, 27–34. [[CrossRef](#)]
25. Brandon, S.; Derby, J.J. Internal radiative transport in the vertical Bridgman growth of semitransparent crystals. *J. Cryst. Growth* **1991**, *110*, 481–500. [[CrossRef](#)]
26. Brandon, S.; Derby, J.J. Heat transfer in vertical Bridgman growth of oxides: Effects of conduction, convection, and internal radiation. *J. Cryst. Growth* **1992**, *121*, 473–494. [[CrossRef](#)]
27. Xiong, H.B.; Ma, Y.; Zheng, L.L. A modified HEM system for optical crystal growth with high melting temperature. *J. Cryst. Growth* **2007**, *299*, 404–412. [[CrossRef](#)]
28. Ma, W.C.; Zhao, L.L.; Ding, G.Q.; Yang, Y.; Lv, T.Z.; Wu, M.; Liu, L.J. Numerical study of heat transfer during sapphire crystal growth by heat exchanger method. *Int. J. Heat Mass Transf.* **2014**, *72*, 452–460. [[CrossRef](#)]
29. Wu, M.; Zhao, W.H.; Liu, L.J.; Yang, Y.; Ma, W.C.; Wang, Y. Effects of crucible cover on heat transfer during sapphire crystal growth by heat exchanger method. *J. Cryst. Growth* **2014**, *404*, 130–135. [[CrossRef](#)]
30. Wu, M.; Liu, L.J.; Yang, Y.; Zhao, W.H.; Ma, W.C. Effect of crucible location on heat transfer in sapphire crystal growth by heat exchanger method. *Heat Transf. Eng.* **2015**, *37*, 332–340. [[CrossRef](#)]
31. Miyagawa, C.; Kobayashi, T.; Taishi, T.; Hoshikawa, K. Development of the vertical Bridgman Technique for 6-inch diameter *c*-axis sapphire growth supported by numerical simulation. *J. Cryst. Growth* **2014**, *402*, 83–89. [[CrossRef](#)]
32. Liu, L.J.; Kakimoto, K. Partly three-dimensional global modeling of a silicon Czochraski furnace. I. Principles, formulation and implementation of the model. *Int. J. Heat Mass Transf.* **2005**, *48*, 4481–4491. [[CrossRef](#)]
33. Chai, J.C.; Lee, H.S.; Patankar, S.V. Finite volume method for radiation heat transfer. *J. Thermophys. Heat Transf.* **1994**, *8*, 419–425. [[CrossRef](#)]
34. Chai, J.C.; Lee, H.S.; Patankar, S.V. Ray effect and false scattering in the discrete ordinates method. *Numer. Heat Transf. B Fund.* **1993**, *24*, 373–389. [[CrossRef](#)]

35. Wu, M.; Liu, L.J. Effect of Angular Discretization on the Radiation Heat Transfer by Finite Volume Method. Science Paper Online, Article No. 201308-72. Available online: <http://www.paper.edu.cn/releasepaper/content/201308-72> (accessed on 8 August 2013).
36. Fainberg, J.; Leister, H.J. Finite volume multigrid solver for thermo-elastic stress analysis in anisotropic materials. *Comput. Methods Appl. Mech. Eng.* **1996**, *137*, 167–174. [[CrossRef](#)]



© 2017 by the authors; licensee MDPI, Basel, Switzerland. This article is an open access article distributed under the terms and conditions of the Creative Commons Attribution (CC-BY) license (<http://creativecommons.org/licenses/by/4.0/>).